REPORT DOCUMENTATION PAGE

The public reporting burden for this collection of information is estimated to average 1 hour per response, including the time for reviewing instructions, searching existing data sources, gathering and maintaining the data needed, and completing and reviewing the collection of information. Send comments regarding this burden estimate or any other aspect of this collection of information, including suggestions for reducing the burden, to Department of Defense, Washington Headquarters Services, Directorate for Information Operations and Reports (0704-0188), 1215 Jefferson Davis Highway, Suite 1204, Arlington, VA 22202-4302. Respondents should be aware that notwithstanding any other provision of law, no person shall be subject to any penalty for failing to comply with a collection of information if it does not display a currently valid OMB control number. **PLEASE DO NOT RETURN YOUR FORM TO THE ABOVE ADDRESS.**

1. REPORT DATE *(DD-MM-YYYY)*	2. REPORT TYPE	3. DATES COVERED *(From - To)*
12102005	Proceeding	

4. TITLE AND SUBTITLE	5a. CONTRACT NUMBER
Application of a New Grain-Based Reconstruction Algorithm to Microtomography Images for Quantitative Characterization and Flow Modeling	5b. GRANT NUMBER
	5c. PROGRAM ELEMENT NUMBER
	0602782N

6. AUTHOR(S)	5d. PROJECT NUMBER
Karsten E. Thompson, Clinton S. Willson, Christopher D. White, Stephanie Nyman, Janok Bhattacharya, Allen H. Reed	5e. TASK NUMBER
	5f. WORK UNIT NUMBER

7. PERFORMING ORGANIZATION NAME(S) AND ADDRESS(ES)	8. PERFORMING ORGANIZATION REPORT NUMBER
Naval Research Laboratory Seafloor Sciences Branch Stennis Space Center, MS 39529	NRL/PP/7430-05-11

9. SPONSORING/MONITORING AGENCY NAME(S) AND ADDRESS(ES)	10. SPONSOR/MONITOR'S ACRONYM(S)
Office of Naval Research 800 North Quincy Street Arlington, VA 22217-5660	ONR
	11. SPONSOR/MONITOR'S REPORT NUMBER(S)

12. DISTRIBUTION/AVAILABILITY STATEMENT

Approved for public release; distribution is unlimited

13. SUPPLEMENTARY NOTES

Society of Petroleum Engineers SPE 95887, October 2005

14. ABSTRACT

X-ray computed microtomography (XMT) is used for high-resolution, non-destructive imaging and has been applied successfully to geologic media. Despite the potential of XMT to aid in formation evaluation, currently it is used mostly as a research tool. One factor preventing more widespread application of XMT technology is limited accessibility to microtomography beamlines. Another factor is that computational tools for quantitative image analysis have not kept pace with the imaging technology itself.

15. SUBJECT TERMS

X-ray computed microtomography

16. SECURITY CLASSIFICATION OF:			17. LIMITATION OF ABSTRACT	18. NUMBER OF PAGES	19a. NAME OF RESPONSIBLE PERSON
a. REPORT	b. ABSTRACT	c. THIS PAGE			Allen Reed
Unclassified	Unclassified	Unclassified	SAR	11	19b. TELEPHONE NUMBER *(Include area code)* 228-688-5473

Standard Form 298 (Rev. 8/98)
Prescribed by ANSI Std. Z39.18

SPE 95887

Application of a New Grain-Based Reconstruction Algorithm to Microtomography Images for Quantitative Characterization and Flow Modeling

Karsten E. Thompson, Louisiana State University, SPE; Clinton S. Willson, Louisiana State University; Christopher D. White, Louisiana State University, SPE; Stephanie Nyman, University of Waikato; Janok Bhattacharya, University of Houston; Allen H. Reed, Naval Research Laboratory - Stennis Space Center

Abstract

X-ray computed microtomography (XMT) is used for high-resolution, non-destructive imaging and has been applied successfully to geologic media. Despite the potential of XMT to aid in formation evaluation, currently it is used mostly as a research tool. One factor preventing more widespread application of XMT technology is limited accessibility to microtomography beamlines. Another factor is that computational tools for quantitative image analysis have not kept pace with the imaging technology itself.

In this paper, we present a new grain-based algorithm used for computer reconstruction and analysis of granular materials (e.g., consolidated or unconsolidated sands), and subsequent network generation. The algorithm differs significantly from other methods because the first step is to extract the fundamental granular structure from a 3D data set, which provides a wealth of information such as grain sizes, aspect ratios, orientations, surface areas, etc. Knowledge of the basic granular structure serves as a foundation for characterizing the void morphology and creating physically representative pore networks. The algorithm is applied to a sample of sandstone from the Frontier Formation in Wyoming, USA, which was imaged using Synchrotron microtomography. Morphologic and flow-modeling results are presented.

Introduction

Subsurface transport processes such as oil and gas production are multiscale processes. The pore scale governs many physical and chemical interactions and is the appropriate characteristic scale for the fundamental governing equations. The continuum scale is used for most core or laboratory scale measurements (e.g., Darcy velocity, phase saturation, bulk capillary pressure, etc.). The field scale is the relevant scale for production and reservoir simulation.

Multiscale modeling strategies aim to address these complexities by incorporating the various relevant length scales. While pore-scale modeling is an essential component of multiscale modeling, quantitative methods are not as well developed as their continuum-scale counterparts. Hence, pore-scale modeling represents a weak link in current multiscale techniques.

The most fundamental approach for pore-scale modeling is direct solution of the equations of motion (along with other relevant conservation equations), which can be performed using a number of numerical techniques. The finite element method is the most general approach in terms of the range of fluid and solid mechanics problems that can be addressed. Finite difference and finite volume methods are more widely used in the computational fluid dynamics community. The boundary element method is very well suited for low-Reynolds number flow of Newtonian fluids (including multiphase flows). Finally, the lattice-Boltzmann method has been favored in the porous-media community because it easily adapts to the complex geometries found in natural materials.

A less rigorous approach is network modeling, which gives an approximate solution to the governing equations. Network modeling of a porous material involves discretization of the pore space into pores and pore throats. Transport is modeled by imposing conservation equations at the pore scale. Network modeling involves two levels of approximation. The first is the representation of the complex, continuous void space as discrete pores and throats. The second is the approximation to the fluid mechanics when solving the governing equations within the networks. The positive trade off for these significant simplifications is the ability to model transport over orders-of-magnitude larger characteristic scales. Consequently, the two approaches (rigorous modeling of the conservation equations versus network modeling) have complimentary roles in the overall context of multiscale modeling. Direct methods will remain essential for studying first-principles behavior and sub-pore-scale processes such as diffusion boundary layers during surface reactions. Network modeling will provide the best avenue for capturing larger characteristic scales (which is necessary for modeling the pore to continuum scale transition).

This research addresses one of the significant hurdles for quantitative network modeling: the use of high-resolution imaging of real materials for quantitative flow modeling. We focus in particular on X-ray computed microtomography (XMT) to obtain three-dimensional pore-scale images, and present a new technique for direct mapping of the XMT data onto networks for quantitative modeling. This direct mapping (in contrast to the generation of statistically equivalent networks) ensures that subtle spatial correlations present in the original material are retained in the network structure.

The specific algorithm described here was designed for the analysis of unconsolidated marine sands,[1] and is being applied for the first time to a consolidated sandstone. The terminology *grain-based algorithm* refers to the fact that the first step in the algorithm is the characterization of the underlying granular structure, which in turn is used to aid in mapping out the pore network structure. The advantage of the grain-based approach is twofold. First, the identification of the granular structure from a voxel-based image is less sensitive to issues such as image resolution as compared to, for instance, the identification of a pore skeleton. Second, knowledge of the granular structure provides important insight into the locations and connections in the pore space, thus providing increased robustness in the network construction algorithm. A side benefit is the speed of the algorithm.

Background

X-Ray Microtomography

X-ray computed microtomography provides nondestructive and noninvasive three-dimensional images of the interior of objects by mapping the X-ray absorption through the sample. The amount of absorption depends on the chemical composition of the material and the energy of X-ray. XMT is based on the reconstruction of the cross-section of an object from its projection data by passing a series of rays through an object, and measuring the attenuation of these rays using detectors placed on the downstream side of the object. Projections are obtained by measuring the X-ray attenuation coefficients of the sample at different angles. These attenuation values are represented in images as discrete elements (pixels in two-dimensional images and voxels in three-dimensional images). Synchrotron radiation has several advantages over traditional X-ray sources including high flux intensity (number of photons per second), high degree of collimation (source divergence leads to image blur), and the ability to tune the photon energy to a single energy or frequency over a wide range using an appropriate monochromator for obtaining specific-element measurements.

Over the last two decades, XMT has played an increasingly important role in the characterization of porous media flow and transport. Due to its non-destructive nature and increasingly high-resolution, synchrotron-based XMT provides the high-quality datasets necessary to capture the 3D microstructure of the media[2-4] and the distribution of fluids within the pore space.[5-7] The ability to characterize and correlate the void space microstructure and fluid distributions provides data to improve and validate pore-scale models..

Network Modeling

Network modeling has a long history in the oil and gas industry beginning with the landmark paper of Fatt.[8] For a long subsequent period, network modeling techniques employed lattice-based networks, usually decorated with a distribution of pore (or pore body in some literature) and pore throat sizes. These lattice based models are valuable for qualitative studies of transport in interconnected, heterogeneous structures. However, they have not proved to be effective for quantitative modeling of real materials.

Beginning in the early 1990s, new techniques were developed for quantitative network modeling. Bryant et al.[9] created physically representative network models from the highly characterized Finney packing.[10] Oren and coworkers created synthetic (computer-generated) sandtones and developed a technique for extracting networks from these structures.[11,12] Their group has continued to develop this approach and the resulting networks have been used by a number of other investigators.[13-15] Lindquist et al. used the medial axes of microtomography images to characterize the pore structure,[16] and this approach was then extended to allow for direct generation of network structures.[17] Thompson and Fogler[18] applied the techniques of Bryant et al.[9] to computer-generated packed beds, and Al-Raoush et al. extended this work to allow for network structures with arbitrary connectivity.[19] Ioannidis and coworkers have used simulated annealing and other algorithms to produce networks that conform to key statistics in real materials.[20-22]

For the network modeling used in this work, we borrow the terminology *physically representative network models*[9] to describe the general class of models, and we note two important characteristics of these structures. First, these networks are a one-to-one mapping of a specific porous material of interest, which ensures that all subtle spatial correlations in the pore structure are retained. Second, the networks are described using rigorous geometric parameters, which ensures that the pore morphology is not compromised despite the need to discretize the pore space. This latter point contrasts with techniques in which the pore structure is transformed into a network of interconnected capillaries from the outset, an approach which has been shown to cause ambiguity in the subsequent modeling of flow.[23]

It should be noted that there is no unique or correct discretization of most real pore structures (exceptions being simples structures such as cubic packings of spheres). Likewise, there is more than one approach that can be taken to describe a network model. In this work, we use the set of parameters shown in Table 1 to describe the network structure. In addition, the network remains linked to the original structure (whether it is a voxel image or a computer-generated material). This ensures that additional characterization could be performed if warranted by a particular modeling algorithm; it would gurantee, in essence, that none of the original morphologic data are lost.

The flow modeling itself is performed by imposing conservation equations at each pore in the network, which results in a set of linear or nonlinear algebraic equations depending on the physics of the process being modeled. A description of the flow modeling algorithms is beyond the scope of the current paper, but this information can be found in many other papers on network modeling.

Table I. Parameters used to describe the network structure.

Variable Association	Variable Name	Variable Type	Dimension
Network	Domain dimensions	vector	length
Pore	Location	vector	length
	Void volume	scalar	$length^3$
	Maximum inscribed radius	scalar	length
Throat	Interconnectivity:periodicity	scalar:vector	
	Cross-sectional area	scalar	$length^2$
	Maximum inscribed radius	scalar	length
	Surface area	scalar	$length^2$
	Hydraulic conductivity	scalar	$length^3$

Dimension on hydraulic conductivity is ^3?

Network Generation from Voxel Data

Despite the advances described in the previous section, what remains surprisingly difficult is the generation of physically representative network models directly from microtomography images of real materials. The difficulty stems from the distinct differences in the form and scale of the data structures. The XMT data consist of hundreds of millions (sometimes billions) of voxels on a Cartesian grid. In contrast, the network representation of the same porous medium is likely to be described using a much smaller data set (order $10^3 - 10^5$ pores), which are interconnected via a complex structure of flowpaths rather than aligned with any specific coordinate system.

Most previous work in this area employs the medial axis as a basis for characterizing the pore structure. For discretized images such as those from XMT, the medial axis is obtained by thinning the original structure until a one-voxel-thick skeleton remains, or by computing distance transforms in the void space (to the void/solid interface) and retaining the skeleton of local maxima. Different medial-axis structures are obtained depending on the method used, the order for thinning, the type of distance transform used, and/or the rules invoked to ensure that topology is retained.[24] Lindquist et al.[25] used the medial axes of 3D images to compute statistical parameters associated with the void space. They later extended their algorithm, using the medial axis as a basis for obtaining pore and throat size distributions, which in turn were mapped onto a network structure.[3] Specifically, the medial axis was trimmed down to the percolating fraction, and nodes were then merged (by comparing the distance separating neighboring nodes to the distance to local surfaces) to define pore locations. Pore throats were found by dilating the medial axis until the dilated cylinder contacted the bounding surfaces; pore-throat geometries were then obtained by triangulating between the medial axis and voxels along the perimeter of the constriction. Sok et el. simulated immiscible displacement on networks generated by this algorithm and compared them to immiscible displacements on regular lattices having identical values for key statistical metrics.[17] Mirroring what Bryant et al.[25] observed for single phase flow, they note that multiphase flow behavior is not reproduced correctly on statistically equivalent networks, emphasizing the need for algorithms that capture true pore morphology. Delerue et al.[26] applied a medial-axis technique to a 3D image of a resin-impregnated soil, and then defined the pore-size distribution in the soil by measuring the maximum inscribed balls for all voxels contained on the skeleton. Mercury intrusion was simulated directly on the voxel map (rather than a network representation). Delerue and Perrier[27] describe in detail the various computational elements used in the algorithm. Silin et al.[28] employed a similar approach, except that the maximal inscribed ball was found for each void-phase voxel in the packing. Though computationally more intensive, this approach allows the pores to be found independently of the skeleton. They tested their algorithm using computer-generated sphere packings and a CT image of Fontainbleau sandstone. However, pore network models were not created, and a quantitative assessment of the pore locations, sizes, and connectivity was not made.

Materials and Methods

Sandstone Sample

The sample used for this application was taken from the Wall Creek Member of the Cretaceous Frontier Formation, Wyoming, USA as part of an integrated geologic, geophysical, and engineering study.[29] Ten wellbores were drilled through the Wall Creek Member and sample plugs were selected. The subject sample is from a tidal facies. The permeability of this sample was severely reduced by calcite cementaion. This reduced the permeability by several orders of magnitude in approximately 15 volume percent of the tidal facies.[30] The sediments preserved in these rocks were derived from uplifts to the north and west. Nyman et al.[30] report that the average composition is approximately 51 percent quartz, 21 percent rock fragments, and 28 percent feldspars, highly altered volcanic components with diagenetic cement dominantly calcite. In uncemented rocks of the tidal facies, porosity averages about 0.22 and permeability is in the range of tens to a few hundred millidarcies, with a mean of 110-140 md (higher for flood-dominated deposits).

XMT of the Sandstone

A sample was impregnated with an epoxy resin under vacuum and then cored to a length of 25 mm and diameter of 5 mm. A 5 mm long section of the core was imaged at 33.07 keV energy at the 13-BMD tomography beamline, operated by GeoSoilEnviroCARS at the Advanced Photon Source. Image reconstruction was performed using algorithms developed by GSECARS to convert CT attenuation data to 3D volumetric data The resultant 3D gray-scale image has a voxel resolution of 7.63 microns. Segmentation, the process of converting a gray-scale image to a 1-bit or binary image by separating the image into two populations based on gray-scale values, was performed using the indicator kriging technique[31] that is part of the 3DMA software package. In this case, the pore voxels are assigned a value of 0 and the grain voxels are assigned a value of 1. Figure 1 is an image of the binary volume file.

While the porosity of the resultant binary image is relatively close to that of the bulk sandstone sample (18.6% versus 22%), the combination of mineralology (i.e,. higher absorbing elements) and X-ray energy created a relatively high signal-to-noise ratio. This less-than-ideal image quality made it difficult to completely resolve the solid and void phases and to remove the ring artifacts. Additional imaging experiments are planned that should produce higher quality datasets. (See concluding comments.)
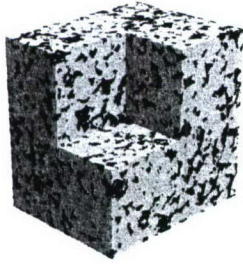
Figure 1. Binary volume file of the sandstone obtained from XMT

Network Construction

Overview

The input for the algorithm is a binary volume file describing the porous material of interest: voxel labels indicate whether the voxel is contained in the void phase or solid phase of the material. The algorithim operates by identifying grains, searching for pores based on the grain locations, and then creating the interconnected network using a novel restricted-burn algorithim. The significant differences between this algorithm and other network generation techniques include the following:

1. The first step in the algorithm is the identification of the granular structure, which is less sensitive to image resolution than processes such as skeletonization. Consequently, networks created for the same material at two different image resolutions have very similar structure and properties.

2. The algorithm uses the granular structure as a template to help define pores. This means that the computationally expensive search for pores becomes linked to the number of grains in the image rather than the number of voxels, and the computational penalty for increasing image resolution is less severe than with other algorithms.

3. Because the grain locations provide the framework for determining pore structure, the algorithm operates without ever computing a skeleton of the pore space. By eliminating this step, a number of problematic issues such as nonuniqueness, dependence on image resolution, and the formation of internal loops are avoided.

3. A key intermediate step is employed between the original binary map and the final network structure, which is the assignment of an integer label to every voxel (both void and solid phase) that denotes the grain or the pore to which that voxel belongs. The reason for emphasizing this intermediate step is that, once it is accomplished, the tasks of obtaining statistical information and constructing the network are straightforward and unambiguous.

Grain Reconstruction Algorithm

Step 1. Dual-Phase Burn. A simultaneous grain-phase and void-phase burn is performed (using the terminology of Lindquist et al.,[16]). Voxels in the solid phase are labeled with

positive integers denoting the burn level and voxels in the void phase are labeled with the negative of the burn level. This convention is not necessary if the burn map remains coupled with the binary material array; however, the use of opposing signs allows the burn numbers to be written over the initial material array without losing the phase information.

Step 2. Location of Extrema. A search is performed to find local maxima in the burn assignments. These local extrema are islands of one or more voxels that are surrounded by voxels with lower burn numbers. In the simplest form of the algorithm, the local maxima are taken to be the grain centers. However, refining the grain locations using optimization leads to better results. Simultaneously, the local minima can be found (which according to the sign convention are in the void phase). In practice, this step is skipped to reduce computation time because the void-phase extrema are not used to define the pore structure. However, the minima are found and reported for completeness in this paper.

Step 3. Tessellation of the grain centers. A periodic Delaunay tessellation is performed using the locations of the grain centers.[32] The purpose of the tessellation is to identify likely pore locations based on the granular structure. The role of the tessellation is somewhat subtle, and the following points are worth clarifying:

1. In contrast to other techniques where the Delaunay tessellation is used to define pore structure,[9,18,19,25] it does not influence the structure of the pores in the current algorithm. In fact, the only restriction that it imposes is on the total number of pores: the algorithm will not find more pores than the number of tetrahedrons in the tessellation. This limitation should not be of practical consequence since the tendency of the Delaunay tessellation is to identify too many pores (by splitting single pores into multiple tetrahedrons; see reference 19). Furthermore, this restriction can be relaxed if necessary at the expense of increased computation time (see item 3).

2. Use of the Delaunay tessellation to aid in the identification of pore locations provides a dramatic advantage as compared to using more traditional erosion/dilation techniques because the number of pores that are located for a given porous medium is relatively insensitive to voxel resolution. This issue is demonstrated later in the validation section.

3. Finally, it should be pointed out that the tessellation is a valuable but not essential part of the algorithm. An alternative approach would be to perform the optimizations described in the next step beginning with every void-phase voxel. However, even for the relatively small sandstone dataset used here, this approach requires solving ~5,000,000 nonlinear optimization problems (in contrast to ~25,000 optimizations when the tessellation is used as a template).

Step 4. Locating pores. In the introduction we note that the division of void space into pores is somewhat arbitrary. In this work, we use the distance function $d(x,y,z)$, whose value gives

the minimum distance from the point [x,y,z] in the void space to a grain surface,[33] and then define a pore as any local maxima in d. In practice, this definition corresponds to a common definition of a pore: locations of maximum-diameter spheres that can be inscribed into the void space, and that are constrained from movement by the surrounding solid phase.[34] In step 4, these maximum-diameter inscribed spheres are located by performing repeated optimization procedures (to maximize d) using the tetrahedrons as seed locations to start the optimizations.

The optimizations themselves are performed using a modified Powell's method,[35] which is a direction set method effective for situations where gradients in the objective function cannot be calculated directly. In essence, the procedure repeatedly performs one-dimensional line minimizations. Various schemes are available to choose the minimization directions, most based on estimating new conjugate directions from the history of the optimization.

As each extremum is found, the voxel containing its x,y,z location is marked with the pore number. If a different seed has already converged to this same voxel (though the coordinate location would rarely be exactly the same), a new pore is not added to the list. Hence, Step 4 ends having generated a list of N pore locations and inscribed radii (i.e., maximum d values), along with N void-phase voxels labeled with the corresponding pore number. At this point, the pores are no longer tied to their seed tetrahedrons, and there is no further need for the Delaunay tessellation in the algorithm.

Step 5. Pore Merging. A viable option is to use all pore locations identified in Step 4, and proceed with constructing the network. However, in real cases, many pores overlap with one another by a significant amount, the overlaps being caused by one of two reasons: 1. the local pore geometry causes two independent extrema to be in proximity; 2. two different seeds have led to the same extremum, but numerical error or optimization tolerances have caused the computed extrema locations to differ by at least one voxel.

In either of the above cases, there is good reason to merge two largely overlapping pores into one. Various merge criteria can be devised. In the current algorithm, pores are merged only if one inscribed sphere encompasses the center of a neighboring inscribed sphere. The location and radius of the larger inscribed sphere is used as a seed, and a local optimization is performed once again to verify the location of the merged pore. With the adjusted pore locations (due to the reoptimization of merged pores), we have found it advisable to make another pass to check whether additional pores should be merged, and indeed to continue this merge → re-optimization procedure iteratively until no more pores are merged. Step 5 ends with the same information as Step 4 (pore locations, radii, and corresponding voxel assignments), but with fewer and more spatially independent pores.

Step 6. Grain and pore assembly. Step 6 is the key intermediate step mentioned in the overview above: the assignment of all voxels in the image to one of the grains or pores identified in Steps 2 or 5 respectively. This step is performed using a novel restricted burn algorithm, which is described in more detail in the context of grain reconstruction

elsewhere.[36] In short, is assmbles a cluster of voxels together that are tied to one of the grain or pore locations respectively, in accordance with the local geometry.

A summary of the logic for this restricted burn procedure (Step 6) is the following:

1. Set the minimum burn level to the largest (absolute) value found in the pore space.

2. Loop through all voxels in the domain.

3. If the current voxel borders a voxel already assigned to a particular pore and its absolute burn level is greater than or equal to the current minimum burn level, assign it to the same pore as the assigned neighbor.

4. If any new voxels were assigned during the last pass, go to (2).

5. If no new voxels were assigned during the last pass, reduce the minimum burn level by 1; go to (2).

Step 7. Pore Morphology and Network Construction. Once Step 6 is complete, determining morphologic parameters and constructing the network is a straightforward process. The total volume of each pore is obtained by summing the volume of all voxels assigned to that particular pore. The inscribed pore radii are already known from the Step-4 and Step-5 computations.

In our definition of network structure, pore throats have no volume but rather are defined by the faces where two pore-elements come into contact. Hence, the pore-throats, like the pores, have rigorous geometric parameters associated with them. The unit normal for the pore-throat interface is found by averaging the orientation of all voxel interfaces associated with the given throat. The total cross-sectional area of the throat is then found by summing the areas of voxel faces at this interface projected onto the local unit normal. (Use of the projected area prevents overestimating the area because of the staircase-like convolutions on the voxel surface.) The inscribed area of the throat is found by determining the largest inscribed sphere whose center is located on the throat interface.

Grain surface area is also assigned as a throat parameter since it affects permeability as well as phenomena such as absorption and chemical reactions on grain surfaces. The surface area is assigned by estimating the surface area for each surface voxel, and then assigning that element of surface to its closest throat. This approach ensures that the surface area is conservative (i.e., the sum of all pore throat surface areas equals the total surface area in the packing), thus providing a good theoretical foundation for its use in modeling.

The last parameter that should be mentioned is the pore-throat hydraulic conductance of each throat, which is necessary for computing permeability and performing dynamic flow simulations. In general, the conductance is computed using some combination of the above-mentioned parameters, via generation of an equivalent capillary. In this work we use the same approach used in Thompson and Fogler.[18] Further work is ongoing to evaluate the best way to compute throat conductivities for various types of materials.

The network itself is defined by mapping out the connectivity of each pore, which is defined by the list of neighboring pores that share voxel-voxel contacts. There are no limitations on the structure of the networks thus obtained (i.e., coordination numbers, etc.), and the resulting network files have exactly the same format as network files from computer-generated media.[23] Once the network is constructed, plots of pore-size distribution, throat-size distribution, coordination number, etc., can be made directly from the data in the network file, without having to return to the large voxelized data sets.

Validation (can you add units for VR etc.?)

The grain-reconstruction algorithm has been tested extensively using computer-generated packings of spheres and cylinders as well as XMT data from unconsolidated particles and sands. Separately, the network-generation algorithm has been tested using a series of computer-generated packings of spheres. This approach is valuable for three reasons: First, the pore structure in the material is known exactly; hence, the validity of the network generation process can be assessed in a quantitative manner. Second, the computer-generated structures can be discretized at arbitrary voxel resolution, which provides good benchmarks for the accuracy that can be expected with data from real materials. Third, the computer-generated data are free from noise and artifacts, which allows validation to be focused solely on the network construction (rather than imaging and segmentation issues).

Three sphere packings were used for validation: a cubic packing, a rhombohedral packing, and a random packing. The two regular packings span the full range of attainable porosities for monodisperse spheres and the pore structure is known exactly. The random packing is more representative of real materials. No single network is correct for the random case. However, the modified Delaunay Tessellation (MDT)

Table II. Notation used to quantify network generation algorithms.

Parameter	Description
A_{cs}	Cross sectional area of a pore throat (ave)
A_s	Surface area assigned to a pore throat (ave)
D_G	Grain diameter (ave)
D_P	Pore diameter (inscribed) (ave)
D_{PT}	Pore-throat diameter (inscribed) (ave)
# EG	Number of extrema in the grain-phase burn
# EV	Number of extrema in the void-phase burn
L_{PT}	Length of pore throat (ave)
MBG	Maximum burn number in the grain phase
MBV	Maximum (absolute) burn number in the void phase
N_G	Number of grains
N_P	Number of pores
PLE	Average error (%) in the computed pore locations
# P_I	Number of pores initially found from the tetrahedron seeds
# PM	Number of one-to-one pore matches (reconstructed packing vs original)
# P_M	Final number of pores after the iterative merging/reoptimization process
# Tet	Number of tetrahedrons used as seeds for pore locations
$V_{F,min}$	Minimum number of voxel faces required for a pore throat to be formed
# Vox	Number of voxels in the data set
V_p	Volume of a pore (ave)
VPD	Voxels per particle diameter
VR	Voxel resolution
Z	Pore coordination number
ε	Porosity

structure and can be used for comparison to the networks generated from the voxelized images.

Table 2 explains the notation used for reporting the statistical results. Selected quantitative data are presented in Table 3. Note that for the three sphere packings, the top row of each section contains parameters obtained from the MDT networks. These parameters are used to quantify the error in the voxel-based parameters. For the cubic and rhombohedral packings, the MDT values agree with theoretical values from a unit-cell analysis, and are exact within the numerical tolerances set in the MDT algorithm. As mentioned above, there exist no "correct" morphologic values for the random packing, but the MDT algorithm is viewed as an excellent benchmark.

Identification of Pores. Column *#EV* is the number of extrema in the void-phase burn. This parameter is the most logical choice for determining pore locations if the burn information were to be used directly. However, notice the very

Table III. Validation of the grain-based network generation algorithm using computer-generated sphere packs.

VR	VPD	# Vox	MBG	MBV	# EG	# EV	# Tet	# P_I	# P_M	D_P ave	D_P sd	V_P ave	V_P sd	# PM	PLE	Z min	Z max	Z ave	D_{PT} ave	D_{PT} sd	A_{cs} ave	A_{cs} sd	A_S ave	A_S sd
Cubic Packing																								
MDT									64	0.7317	0	0.4764	0			6	6	6	0.4142	0	0.5227	0	1.0472	0
0.100	10.0	40×40×40	3	2	64	64	458	215	64	0.6996	0.0003	0.4480	0	64/64	0.07%	6	6	6	0.3772	0	0.5046	0	0.9037	0.0367
0.096	10.3	41×41×41	3	3	64	64	443	201	64	0.7141	0.0308	0.4512	0.0526	64/64	6.93%	6	13	6.94	0.3960	0.0886	0.4506	0.1416	0.7334	0.2049
0.090	11.0	44×44×44	4	2	64	64	458	218	64	0.7190	0.0104	0.4583	0.0248	64/64	0.09%	6	6	6	0.4650	0.0454	0.5097	0.0221	0.8442	0.0443
0.080	12.5	50×50×50	4	3	64	64	459	139	64	0.7190	0.0302	0.4788	0.0120	64/64	0.08%	6	6	6	0.4519	0.0260	0.5357	0.0157	0.9087	0.0345
0.050	20.0	80×80×80	6	4	64	64	458	270	64	0.7428	0.0000	0.4720	0	64/64	0.06%	6	6	6	0.4078	0	0.5171	0	0.9247	0.0404
0.047	21.3	85×85×85	7	5	64	64	418	157	64	0.7189	0.0119	0.4742	0.0082	64/64	2.37%	6	12	6.66	0.3856	0.0978	0.4766	0.1399	0.8594	0.2069
0.020	50.0	200×200×200	14	11	64	64	458	187	64	0.7366	0.0001	0.4740	0	64/64	0.05%	6	6	6	0.4184	0	0.5166	0	0.9920	0.0164
0.010	100.0	400×400×400	29	21	64	64	458	194	64	0.7261	0.0000	0.4760	0	64/64	0.05%	6	6	6	0.4198	0	0.5220	0	1.0093	0.0095
Rhombohedral Packing																								
MDT									192	0.2878	0.0892	0.0612	0.0498			4	8	5.33	0.1547	0	0.2266	0	0.3927	0.0585
0.100	10.0	40×34×32	3	2	64	4	384	277	177	0.3374	0.0503	0.0607	0.0365	167/192	41.40%	2	20	6.71	0.2310	0.0437	0.1761	0.0457	0.2232	0.0603
0.060	16.7	66×57×54	5	2	64	160	384	261	192	0.2994	0.0742	0.0599	0.0472	192/192	23.02%	1	20	6.38	0.1795	0.0205	0.1827	0.0410	0.2688	0.0792
0.040	25.0	100×86×81	8	4	64	88	384	271	192	0.2922	0.0786	0.0598	0.0470	192/192	18.04%	2	19	6.41	0.1489	0.0309	0.1862	0.0560	0.2785	0.0976
0.020	50.0	200×173×163	15	6	64	192	384	320	192	0.2875	0.0836	0.0608	0.0491	192/192	6.80%	1	26	6.60	0.1339	0.0421	0.1877	0.0705	0.2958	0.1080
0.015	66.7	226×230×217	20	9	64	251	384	295	192	0.2863	0.0846	0.0607	0.0493	192/192	6.38%	1	30	6.25	0.1266	0.0500	0.1788	0.0808	0.2863	0.1161
0.010	100.0	400×346×326	29	13	64	328	384	276	192	0.2901	0.0999	0.0605	0.0493	192/192	4.14%	1	31	6.10	0.1301	0.0505	0.1885	0.0785	0.3057	0.1094
Random Sphere Packing																								
MDT									409	.3591	0.0921	0.0784	0.0782			3	12	4.6	0.2631	0.0857	0.3541	0.0940	0.3350	0.1220
0.100	10.0	43×43×43	3	3	100	63	615	489	301	.3975	0.0946	0.1063	0.1069	271/409	40.47%	2	20	6.71	0.2900	0.0767	0.2620	0.1214	0.2471	0.1296
0.050	20.0	87×87×87	6	6	100	127	619	562	346	.3559	0.0930	0.0926	0.1005	311/409	26.79%	1	20	6.38	0.2334	0.0900	0.2649	0.1351	0.2563	0.1386
0.040	25.0	109×109×109	8	7	100	155	619	581	369	.3461	0.0968	0.0868	0.1059	310/409	23.46%	2	19	6.41	0.2231	0.0921	0.2566	0.1380	0.2441	0.1428
0.025	40.0	175×175×175	12	11	100	278	620	599	376	.3402	0.0942	0.0853	0.1088	322/409	23.40%	1	26	6.60	0.2083	0.1015	0.2484	0.1479	0.2392	0.1448
0.010	100.0	438×438×438	29	27	100	670	619	611	401	.3309	0.0977	0.0800	0.1331	334/409	21.44%	1	30	6.25	0.1937	0.1100	0.2240	0.1583	0.2424	0.1518
0.008	125.0	548×548×548	37	34	100	803	619	612	407	.3334	0.0959	0.0788	0.1312	350/409	22.90%	1	31	6.10	0.1948	0.1142	0.2185	0.1643	0.2455	0.1527

algorithm[19] is a farily rigorous method for extracting the pore

strong dependence of these values on image resolution (at

least for the non-cubic structures). For the rhombohedral packing, the number of void-phase extrema varies from 4 to 328 as image resolution is varied over an order-of-magnitude (the true number of pores is 192). For the random packing, #EV varies between 63 and 803 as resolution varies from 10 VPD to 125 VPD (the best estimates for number of pores in this packing are ~ 400). Clearly, the void-phase burn provides a poor indicator of pore location, which is related to the problems with skeletonization that were mentioned previously.

In the current algorithm, the grain structure is used as a template for determining pore locations. The initial seeds for pore locations are based on a Delaunay tessellation of the grain locations. Table 3 lists the number of Delaunay tetrahedrons (see column #Tet). The number of largest-inscribed-spheres obtained from these seeds is listed in column $\#P_I$. Note that the numbers in both of these columns are relatively insensitive to image resolution since they are tied to the grain structure rather than the voxel structure.

Focusing on the cubic packing, note that there are significantly fewer inscribed spheres (i.e., pores) found than seeds. The reason for this difference is that to assemble a cubic pore requires at least five tetrahedrons. If the optimization routine were exact, all five seeds would converge on the same central pore location. In reality, more than one seed will usually converge on the same central voxel, and is listed only once. The fact that $\#P_I$ decreases with increasing resolution is somewhat counterintuitive (because higher resolutions provide many more voxels for the optimization to land in). However, the reason for this effect is the increased accuracy of the optimization procedure as resolution increases (which is a consequence of more precise distance-to-surface calculations).

The more important value is the final number of pores after merging ($\#P_M$). For the cubic packing, this value is exact for all resolutions. For the rhombohedral packing, it is exact for resolutions of 16.7 VPD and above. For the random packing, an exact number of pores can never be defined unequivocally. However, the values obtained from the current algorithm and the MDT algorithm agree reasonably well. Results from the random packing also illustrate the efficiency of the grain-based approach. Examining the number of tetrahedrons (each of which generates a seed point to search for a pore) shows that ~ 620 nonlinear optimization procedures were performed to find the initial pore locations, independent of image resolution. In contrast, ~ 32 million of these same computations would have been required for the 100 VPD image if each void-phase voxel were tested to find its maximum inscribed sphere.

Accuracy of Pore Locations. The pore location is defined as the center of the largest sphere that can be inscribed into a given void space. For the cubic packing, the results are essentially exact in cases where an integer VPD value is used. Even in the non-integer-VPD cases, the error remains low. The rhombohedral packing is a much more rigorous test since the pores are not symmetric with respect to the Cartesian voxel grid and also because they are small. The error in pore locations is significant at low resolutions (where pore dimensions can be as small as a single voxel), but it appears to decrease monotonically with increasing voxel resolution.

Table IV. Effect of constraining pore-throat connections

	PORE-THROAT PARAMETERS								
VF_{min}	Z			D_{PT}		A_{CS}		A_S	
	min	max	ave	ave	sd	ave	sd	ave	sd
MDT	2	12	4.60	0.2627	0.0846	0.3548	0.0963	0.3369	0.1233
0	1	26	6.60	0.2083	0.1015	0.2484	0.1479	0.2392	0.1448
1	1	26	6.60	0.2083	0.1015	0.2484	0.1479	0.2392	0.1448
2	1	23	6.08	0.2215	0.0950	0.2673	0.1386	0.2607	0.1475
3	1	21	5.87	0.2269	0.0921	0.2757	0.1338	0.2697	0.1477
4	1	20	5.71	0.2310	0.0898	0.2820	0.1299	0.2770	0.1472
5	1	20	5.71	0.2310	0.0898	0.2820	0.1299	0.2770	0.1472
10	1	19	5.24	0.2422	0.0842	0.3019	0.1164	0.3018	0.1414
50	1	18	4.67	0.2523	0.0814	0.3251	0.1008	0.3386	0.1255
63	0	17	4.57	0.3113	0.0960	0.2981	0.1536	0.3108	0.1792

The accuracy for the random packing is somewhat harder to assess, mostly because the number of pores found does not agree exactly for the MDT versus voxel-based networks. Column #PM in Table 3 provides statistics for the fraction of pores with a one-to-one match with the MDT network (defined when the center of one and only one pore from the voxel network lies inside an inscribed pore of the MDT network). Also shown is the average error in pore location for these one-to-one matches.

Coordination number. Determining the pore coordination number (the number of throats emanating from a pore and connecting to other pores) remains the biggest problem for the algorithm. For the cubic packing, the coordination number is exact for integer VPD values, again due to the fact that pore boundaries are coincident with voxel boundaries. For resolutions that produce non-integer VPD values, the average coordination numbers are slightly higher and the maximum coordination numbers are significantly higher than they should be. The problem is illustrated in Figure 2, which shows two pores assembled from a cubic packing with a non-integer resolution of 21.3 VPD. Although they are constructed correctly (within the limitations of the voxel resolution), the fact that the pore boundaries are not coincident with voxel boundaries creates a contact between two voxel faces at a position that should be a corner-corner contact in reality (and therefore should not register as a throat connection). The numbers from the non-integer VPD cases indicate that this problem occurs less often than once per pore on average (though certain pores are assigned many extra neighbors, as evidence by the high values for the maximum coordination numbers). For the rhombohedral packing, the problem is similar, though no resolution generates the exact coordination pattern since the rhombohedral pore boundaries never lie along voxel boundaries.
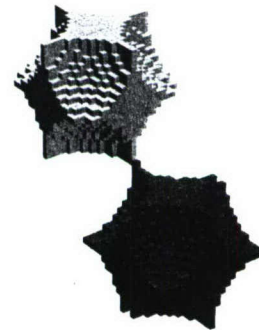

Figure 2. Non-physical pore throat connection in a cubic packing of spheres.

For random pore structures the problem is exacerbated. The pore geometries are more irregular (anomalies are not limited to corner-corner contacts as with the cubic packing) and, like the rhombohedral packing, the Cartesian voxel system does not allow for perfect breaks in the pore geometry. Estimates of average pore coordination number fall into the mid-sixes range. These values are probably too high, again because of identification of voxel-voxel connections that should not register as pore-pore connections (a fact also evidenced by the large values of maximum coordination number).

The obvious solution to this problem is to set a minimum limit for the number of voxel-voxel connections that constitutes a pore throat. For the cubic packing, requiring pore throats to be composed of three-or more voxel faces led to perfect coordination numbers at all non-integer resolutions tested. For the 40 VPD random packing, Figure 3 shows a histogram of the number of voxel faces found in a throat connection. The histogram has a broad minimum before the population begins to increase at around 70 voxel-faces/throat. Interestingly, the theoretical minimum for throat size at this resolution is 64 voxel-faces/throat, which lends credence to the histogram. These two factors suggest that connections made at less-than ~64 voxel-faces/throat are anomalies and should be discarded. Table 4 shows the results for various minimum-voxel limits applied to the 40 VPD random sphere packing. For a conservative minimum of 50 voxel-faces/throat, the revised throat parameters are in much better agreement with the MDT values, with the average pore coordination number reduced to 4.67. A more aggressive limit of 63 voxel-faces per throat caused the values to deteriorate, indicating that real throats are being discarded with this higher limit.

Unfortunately, it is difficult to generalize an effective rule for how to limit interconnectivity. Creating a Figure-3-type histogram on a case-by-case basis is a sensible and fairly easy approach with an automated algorithm. However, initial tomographic data from real materials that we have tested do not show the bimodal distribution found in Figure 3 and therefore do not provide a strong rationale for a cutoff value.
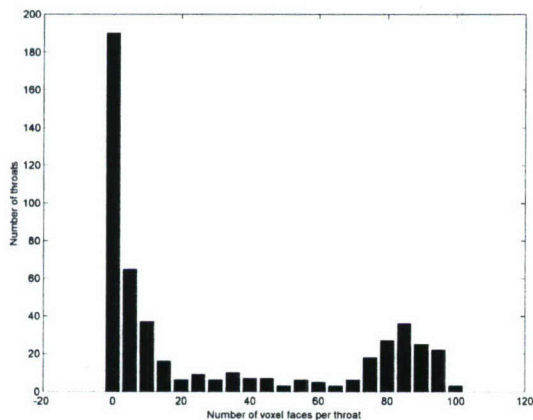
throats will have negligible effect on most transport processes (due to their very small size), and because one risks eliminating what the tomography has identified as 'real' connections. For the purposes of statistical analysis, the extra throats do cause a problem because they affect the calculation of coordination number and average throat parameters. In these cases it is worth the extra effort to assess the distribution of voxel contacts, and provide a cutoff if a case can be made to do so. A final point is that the use of geometric averages should improve the statistical characterization even in cases where small throats are mistakenly identified.

Results

Two different network reconstructions have been performed on the volume data shown in Figure 1. The first uses the grain-reconstruction algorithm. For comparison, a second run was performed in which the search for pores was performed directly on the void-phase voxels, without use of the grain reconstruction and the Delaunay tessellation.

All runs were performed on IBM Power5 8-way p575 machines housed at LSU's high-performance computing center.

Morphologic Parameters

Figure 4 contains an image of the grain reconstruction, which is included for general interest. Colors are assigned randomly to grain numbers to give a visual indication of the discretization into individual grains. (The missing piece at the bottom left corner is an artifact caused by limitations in the graphics software.)

In previous tests of the algorithm on tomography images of unconsolidated sands, two problems with the grain reconstruction process were identified. The first problem is single grains being "broken" into more than one piece. This problem is associated with noise in the data and/or the misidentification of grain centers (which in turn stems from either unusual grain shapes or limitations in the voxel resolution and resulting burn). The second problem is the opposite situation: the identification of a single large grain that
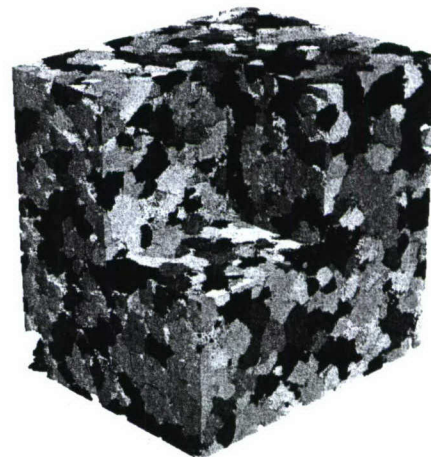

Figure 3. Histogram of the number of pore-throat voxels in a random packing of spheres.

We suggest the following approach. For the purposes of network generation, no cutoff should be used because extra

Figure 4. Grain reconstruction of the Figure-1 data set.

should probably be broken into more than one piece (although this decision is subjective if any level of consolidation is

— **Table V. Morphologic and flow simulation results**

	Grain-Based Network	Voxel-Based Network
N_G	2,334	
D_G (μm)	101	
N_P	10,768	65,574
D_P (μm)	34	18
D_{PT} (μm)	31	26
L_{PT} (μm)	77	35
Z	3.21	3.16
ε	0.186	0.187
K_{xx} (mD)	410	430
K_{yy} (mD)	530	570
K_{--} (mD)	320	360

present). Both of these problems appear to be more pronounced for the current sandstone data as compared to the cleaner data sets available for the unconsolidated sands. Solutions to these problems have been implemented in the algorithm, but are currently undergoing validation tests and so were not used in the current work.

Fortunately, the main problem with the current image appears to be the division of single grains into more than one piece, which will not affect the network generation process in a detrimental way; an increased number of grains will simply cause the algoriththm to search for more pores. However, the final pore locations are determined by the optimization procedure and reflect local geometry regardless of whether the local grains were reconstructed in a reasonable way. Hence, the grain-based algorithm generates a physically representative network even if problems occur in the grain reconstruction process.

Table 5 contains selected parameters generated by the algorithm for the two different network generation techniques. Figure 5 shows histograms of the inscribed pore-size, inscribed pore-throat-size, and pore coordination number for the grain-based network. Figure 6 shows network structure from the same central region of the sandstone, but for the two different networks.

The most striking difference between the two networks is the number of pores, with the grain-based network having many fewer pores and thus longer pore throats spanning the gaps between the pores. This is a consequence of the logic in the grain-based algorithm, which uses the Delaunay tessellation of the grains as seed locations for potential pores. In contrast, the voxel-based algorithm searches for pores from

inscribed spheres). Although the difference in pore numbers is extreme, it is still not possible to declare one network more correct than the other because discretization of the pore space is an arbitrary process (within reason of course). The key is that in for both cases the network is a one-to-one mapping of the pore structure and in both cases the pores are defined using the same rigorous definition: a local maximum in the distance-to-a-grain-surface function. The most effective illustration of these points is to examine the two networks side by side as in Figure 6 and note that, despite differences in the details, the trends in network structure are the same (the appearance of large pores at the same locations; gaps in the network structure at the same locations).

The other notable point from the data presented here is the relatively small difference between the pore-throat diameters and the pore diameters, which is a consequence of the channel like structure in consolidated sands. In fact, in the voxel-based network, the average pore size is smaller than the average throat size. Although this is counter to the traditional pore and pore-throat model, it is simply a consequence of the high density of pores in the second network. This high pore density causes the void space to be defined as strings of largely overlapping pores (rather than distint pores connected by long throats), in which case a pore-throat diameter is simply the size of the channel at the point where two inscribed spheres overlap, and thus is not necessarily smaller than one or both of the adjacent pores.

Flow Modeling

The two networks were used to model single-phase low-Reynolds-number flow of a Newtonian fluid. The flow modeling was performed after cropping 100 μm from all sides of the networks so as to avoid edge effects that are caused by the boundary of the volume data.

Pressure gradients were imposed in one of the coordinate directions and the resulting volumetric flowrates were computed. Permeabilty was then calculated using Darcy's law. The ability to obtain dimensional permeability values is a consequence of using physically representative networks. That is, the network is a map of a specific region of the sandstone, which allows for the computation of dimensional volumetric
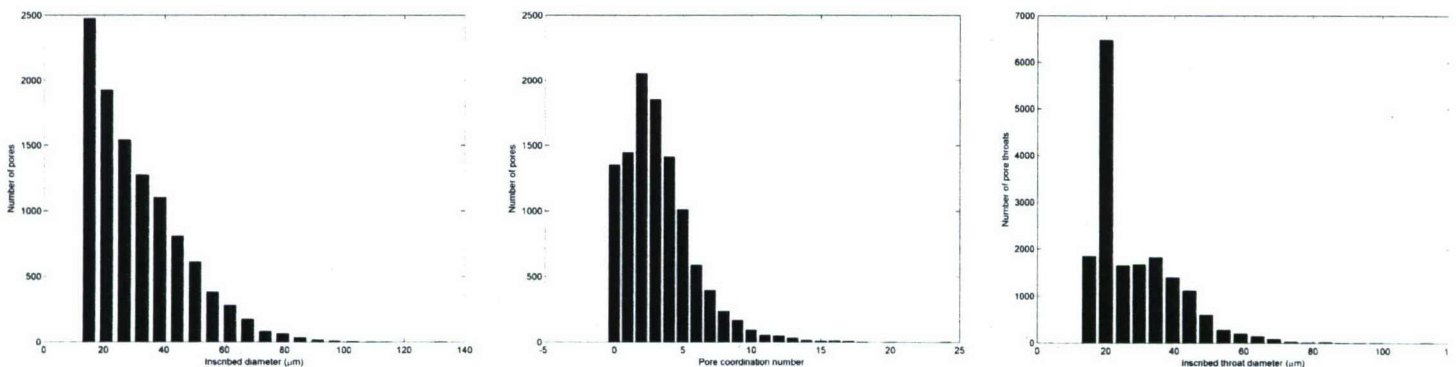

Figure 5. Morphology of the pore space in the sandstone: (a) pore-size distribution (inscribed); (b) pore-coordination-number distribution; (c) pore-throat-size distribution (inscribed).

each voxel location, which results in the identification of many more local extrema (i.e., locations of maximum

flowrates, cross-sectional areas for flow, etc. Additionally, because of the one-to-one mapping, the model has no
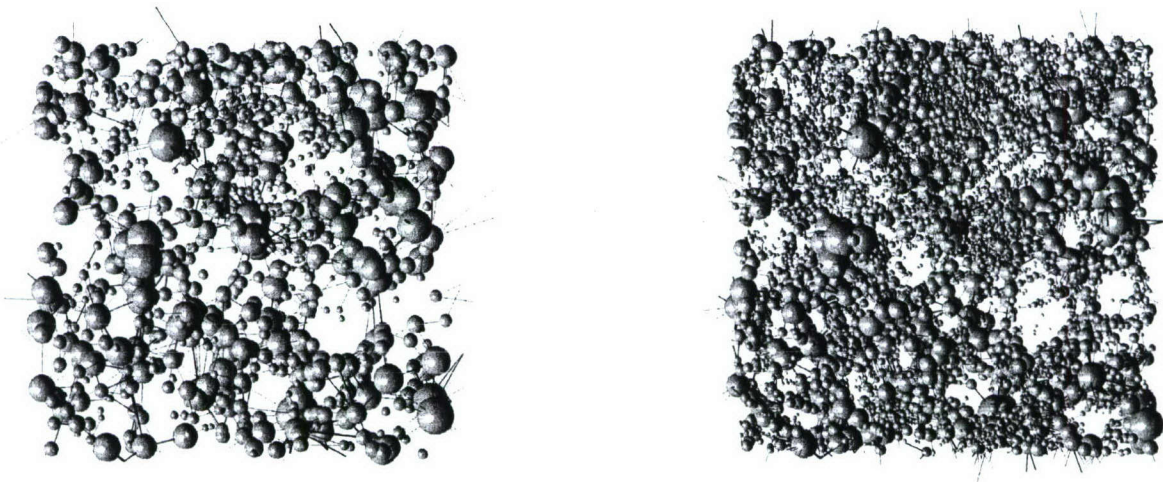
Figure 6. Comparison of a section of the grain-based network (left) to the same section of material in the voxel-based network (right)

adjustable or scaling parameters. (The pore-throat hydraulic conductivities are determined using the formulas developed for sphere packings in reference,[18] and thus are not treated as adjustable parameters.)

The similarity in permeabilities for the two different networks may be surprising considering the different network structures. However, this fact is again a consequence of using physically representative networks: in the network with fewer pores and pore throats, the throats are shorter and therefore have larger hydraulic conductivities. Put simply, everything comes out in the wash.

Figure 7 is a color mapping of single phase flow through the grain-based network (cropped as described above). The
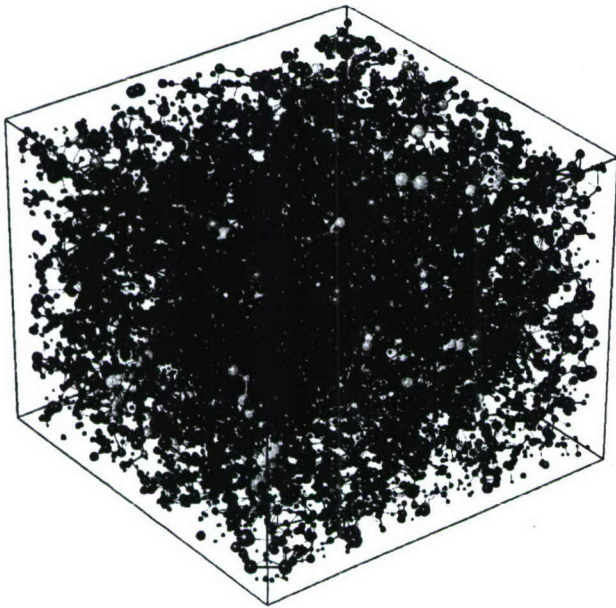

Figure 7. Color representation of single-phase flow through a physically representative network model of the sandstone.

colors are mapped according to volumetric flowrate, with brighter colors indicating high flowrates and the blues indicating low. This graphic shows clearly the heterogeneity in the flow patterns that results from the pore morphology, and demonstrates the rule of thumb that relatively few pores carry a large fraction of the fluid. This graphic is also an effective illustration of the rationale for using network modeling as opposed to simpler effective medium or bundle-of-tubes

models. Although these simpler models may well predict correct permeabilities given the proper pore statistics, they do not capture the flow heterogeneity that contributes strongly to processes such as solute dispersion.

Concluding Comments

It is worth reemphasizing that the 3D image data used in this work contains more noise and imaging artifacts than we are comfortable with in the context of performing quantitative modeling. Thus, the spirit of this research is to develop powerful and robust methods for network generation from binary volume data, and to understand the implications of decisions such as the technique used for pore identification.

Already, x-ray tomography has become a much more accessible technology than only a decade ago, and there is little question that imaging techniques will continue to improve rapidly. This underscores the importance of developing computational tools such as the algorithm described here.

Acknowledgements

References

1. Reed, A.H., K.E. Thompson, C.S. Willson, K.B. Briggs, M.D. Richardson, and B.T. Heffner, "Quantification of sediment properties and geoacoustic parameters from pore structure and grain contacts: A microcomputed tomography analyisis of SAX04 sands," proceedings of the Conference on Boundary Influences in High-Frequency, Shallow Water Acoustics, University of Bath, Sept. 5-9, 2005.

2. Liang, Z., Ioannidis, M.A., Chatzis, I., "Geometric and topological analysis of three-dimensional porous media: Pore space partitioning based on morphological skeletonization." *J. Colloid Interface Sci.* **221**, 13-24 (2000).

3. Lindquist, W.B., A. Venkatarangan, J. Dunsmuir and T-f Wong, "Pore and throat size distributions measured from synchrotron X-ray tomographic images of Fontainebleau sandstones," *J. Geophys. Res.*, **105**(B9), 21509-21527 (2000).

4. Al-Raoush, R.I., and C.S. Willson, "Extraction of Physically-Representative Pore Network from Unconsolidated Porous Media Systems Using Synchrotron Microtomography," *Journal of Hydrology* **300** (1-4), 44-64 (2005).

5. Seright, R.S., J.-T. Liang, W.B. Lindquist, and J.H. Dunsmuir, "Characterizing disportation permeability reduction using synchrotron X-ray computed tomography," *SPE Res. Eval. Eng.* **5**, 355-364 (2002).

6. Seright R.S., J.-T. Liang, W.B. Lindquist, and J.H. Dunsmuir, "Use of X-ray computed microtomgraphy to understand why gels reduce permeability to water more than to oil," *J. Pet. Sci. Eng.* **39**, 217-230 (2003).

7. Al-Raoush, R.I., Willson, C.S., 2005, A Pore-scale Investigation of a Multiphase Porous Media System, *J. Contam. Hydrology* . 77 (1-2), 67-89

8. Fatt, I., "The network model of porous media: I. Capillary pressure characteristics," *Pet. Trans. AIME*, **207**, 144-159 (1956).

9. Bryant, S.L., D.W. Mellor, and C.A. Cade, "Physically Representative Network Models of Transport in Porous Media," *AIChE J.*, **39**(3), 387-396 (1993).

10. Finney, J.L., "Random packings and the structure of simple liquids I. The geometry of random close packing," *Proc. Roy. Soc. Lond.* A. **319**, 479-493 (1970).

11. Bakke, S., and P.E. Oren, "3-D Pore-Scale Modelling of Sandstones and Flow Simulations in the Pore Networks, *SPEJ*, **2**(2), 136-149 (1997).

12. Oren, P.-E., S. Bakke, and O.J. Arntzen, "Extending Predictive Capabilities to Network Models," *SPE J.*, **3**(4), 324-336 (1998).

13. Patzek, T.W., "Verification of a complete pore network simulator of drainage and imbibition," *SPE Journal*, **6**(2), 144-156 (2001).

14. Lopez, X., Valvatne, P.H., and M.J. Blunt, "Predictive network modeling of single-phase non-Newtonian flow in porous media," *J. Colloid Interface Sci.*, **264**(1), 256-265 (2003).

15. Valvatne, P.H., and M.J. Blunt, "Predictive pore-scale network modeling," paper SPE 84550 presented at the Annual Technical Conference and Exhibition, Denver, CO, Oct. 5-8, 2003.

16. Lindquist, W.B., S.-M. Lee, D.A. Coker, K.W. Jones, and P. Spanne, "Medial axis analysis of void structure in three-dimensional tomographic images of porous media," *J. Geophys. Res.*, **101**(B4), 8297-8310 (1996).

17. Sok, R.M., M.A. Knackstedt, A.P. Sheppard, W.V. Pinczewski, W.B. Lindquist, A. Venkatarangan, and L. Paterson, "Direct and stochastic generation of network models from tomographic images; effect of topology on residual saturations," *Transport in Porous Media*, **46**, 345-372, 2002.

18. Thompson, K.E., and H.S. Fogler, "Modeling Flow in Disordered Packed Beds from Pore-Scale Fluid Mechanics," *AIChE J.*, **43**(6), 1377 (1997).

19. Al-Raoush, R., K.E. Thompson, and C.S. Willson, "Comparison of network generation techniques for unconsolidated porous media," *Soil Sci. Soc. Am. J.* **67**, 1687-1700 (2003).

20. Talukdar, M.S., O. Torsaeter, M.A. Ioannidis, and J.J. Howard, "Stochastic reconstruction, 3D characterization and network modeling of chalk," *J. Pet. Sci. Tech.*, **35**(1-2), 1-21 (2002)

21. Liang, Z., M.A. Ioannidis, and I. Chatzis, "Permeability and electrical conductivity of porous media from 3D stochastic replicas of the microstructure," *Chem. Eng. Sci.*, **55**, 5247-5262 (2000).

22. Ioannidis, M.A., M.J. Kwiecien, I. Chatzis, I.F. MacDonald, and F.A.L. Dullien, "Comprehensive pore structure characterization using 3D computer reconstruction and stochastic modeling," paper SPE 38713 presented at the Annual Technical Conference and Exhibition, San Antonio, Oct. 5-8 (1997).

23. Balhoff, M., and K.E. Thompson, "Modeling the steady flow of yield-stress fluids in packed beds," *AIChE J.* **50**(12), 3034-3048 (2004).

24. Lohman, G. *Volumetric Image Analysis* (John Wiley & Sons, New York, 1998).

25. Bryant, S.L., P.R. King and D.W. Mellor, "Network model evaluation of permeability and spatial correlation in a real random sphere packing," *Transport in Porous Media*, 11, 53-70 (1993).

26. Delerue, J.F., E. Perrier, Z.Y. Yu and B. Velde, "New algorithms in 3D image analysis and their application to the measurement of a spatialized pore size distribution in soils," *Phys. Chem. Earth (A)* **24**(7), 639-644 (1999).

27. Delerue, J.-F. and E. Perrier, "DXSoil, a library for 3D image analysis in soil science," *Computers & Geosciences*, 28, 1041-1050 (2002).

28. Silin, D.B., G. Jin and T.W. Patzek, "Robust determination of the pore space morphology in sedimentary rocks," paper SPE 84296 presented at the Annual Technical Conference and Exhibition, Denver, CO, Oct. 5-8, 2003.

29. Gani

30. Nyman

31. Oh, W., and W. B. Lindquist, „Image thresholding by indicator kriging." *IEEE. Transactions on Pattern Analysis and Machine Intelligence*, **21**, 590-601 (1999).

32. Thompson, K.E., "Fast and robust Delaunay tessellation in periodic domains," *Int. J. Numer. Meths. Eng.*, **55**, 1345-1366 (2002).

33. Luchnikov, V.A., N.N. Medvedev, L. Oger and J.-P. Troadec, "Voronoi-Delaunay analysis of voids in systems of nonspherical particles," *Phys. Rev. E*, **59**(6), 7205-7212 (1999).

34. Scheidegger, A.E., *The Physics of Flow Through Porous Media*, 3rd Ed. (University of Toronto Press, 1974).

35. Press, W.H., S.A. Teukolsky, W.T. Vetterling and B.P. Flannery, *Numerical Recipes in Fortran 77*, 2nd Edition (Cambridge University Press, 1992).

36. Thompson, K.E., C.S. Willson, and W. Zhang, "Quantitative computer reconstruction of particulate materials from microtomography images," (in review, 2005).